



Article

Waste-to-Resource Strategy to Fabricate Functionalized MOFs Composite Material Based on Durian Shell Biomass Carbon Fiber and Fe₃O₄ for Highly Efficient and Recyclable Dye Adsorption

Zhangzhen Cai ^{1,†}, Qi Liu ^{1,†}, Haoxin Li ¹, Jingyi Wang ¹, Guoyu Tai ¹, Fan Wang ¹, Jiangang Han ^{1,*}, Yongli Zhu ¹ and Guangyu Wu ^{1,2,*} 

¹ Co-Innovation Center for the Sustainable Forestry in Southern China, College of Biology and the Environment, Nanjing Forestry University, Nanjing 210037, China; caizznjfu@126.com (Z.C.); liuqichem@126.com (Q.L.); lihaoxinnjfu@126.com (H.L.); wangjychem@126.com (J.W.); taigynj@126.com (G.T.); w1032365184@163.com (F.W.); lyly1262011@126.com (Y.Z.)

² Guangxi Key Laboratory of Petrochemical Resource Processing and Process Intensification Technology, School of Chemistry and Chemical Engineering, Guangxi University, Nanning 530004, China

* Correspondence: hjg@njfu.edu.cn (J.H.); gywuchem@njfu.edu.cn (G.W.)

† These authors contributed equally to this work.



Citation: Cai, Z.; Liu, Q.; Li, H.; Wang, J.; Tai, G.; Wang, F.; Han, J.; Zhu, Y.; Wu, G. Waste-to-Resource Strategy to Fabricate Functionalized MOFs Composite Material Based on Durian Shell Biomass Carbon Fiber and Fe₃O₄ for Highly Efficient and Recyclable Dye Adsorption. *Int. J. Mol. Sci.* **2022**, *23*, 5900. <https://doi.org/10.3390/ijms23115900>

Academic Editor: Carlo Crescenzi

Received: 25 March 2022

Accepted: 23 May 2022

Published: 24 May 2022

Publisher's Note: MDPI stays neutral with regard to jurisdictional claims in published maps and institutional affiliations.



Copyright: © 2022 by the authors. Licensee MDPI, Basel, Switzerland. This article is an open access article distributed under the terms and conditions of the Creative Commons Attribution (CC BY) license (<https://creativecommons.org/licenses/by/4.0/>).

Abstract: Recently, metal–organic frameworks (MOFs), which are porous inorganic–organic hybrid materials consisting of metal ions (clusters or secondary building units) and organic ligands through coordination bonds, have attracted wide attention because of their high surface area, huge ordered porosity, uniform structural cavities, and excellent thermal/chemical stability. In this work, durian shell biomass carbon fiber and Fe₃O₄ functionalized metal–organic framework composite material (durian shell fiber-Fe₃O₄-MOF, DFM) was synthesized and employed for the adsorption removal of methylene blue (MB) from wastewater. The morphology, structure, and chemical elements of the DFM material were characterized by scanning electron microscope (SEM), X-ray diffraction (XRD), transmission electron microscope (TEM), and X-ray photoelectron spectroscopy (XPS) techniques. Adsorption conditions such as pH, adsorption time, and temperature were optimized. The adsorption isotherm and kinetics results show that the adsorption process of DFM material to MB is more in line with the Freundlich model and pseudo-second-order kinetic model. Using these models, the maximum adsorption capacity of 53.31 mg/g was obtained by calculation. In addition, DFM material could be easily reused through an external magnet and the removal rate of MB was still 80% after five adsorption cycles. The obtained results show that DFM composite material, as an economical, environmentally friendly, recyclable new adsorbent, can simply and effectively remove MB from wastewater.

Keywords: biomass fibers; durian shell; magnetic composite; adsorption

1. Introduction

With the development of industry, the increase of organic pollutants in wastewater will have various adverse effects on the environment, so more effective treatment methods need to be explored [1,2]. Methylene blue (MB) is an organic dye commonly used in the textile, leather, printing, and dyeing industries. Because of its high chroma and large organic content, if it is directly discharged into the surroundings without treatment, it will endanger the physical and mental health of the human body, causing people to have rapid heartbeat, nausea, and vomiting and, in serious cases, causing cancer. [3]. I methylene blue enters water, it will lead to poor light transmittance and affect the growth of plants and animals in

water [4]. Common water-treatment technologies include flocculation precipitation, membrane separation, photocatalysis, biological methods, and ion exchange [5–14]. Compared with several other treatment technologies, the adsorption method has the advantages of high treatment efficiency, simple operation, no by-products, and recyclability, making it one of the important methods in pollutant treatment [15]. Commonly used adsorbents include activated carbon, molecular sieves, silicone, and zeolite [16], however, these adsorbents are difficult to recycle and the effect of reuse is poor [17,18]. So, designing a new adsorbent with a simple method, easy separation, and good chemical/physical stability is important.

Biomass is a general term for organisms that come directly or indirectly from various plants, with the most extensive source being agricultural and forestry waste [19–21]. The common biomass treatment methods include incineration and burial. These treatment methods not only waste resources, but also cause other environmental pollution problems [22,23]. Durian shell is a type of agricultural and forestry waste. The main components are cellulose, hemicellulose, and lignin. It is a good material for the preparation of biomass adsorbents [24]. However, most of the common adsorbents prepared from durian shells have the disadvantages of large particle size and difficulty in recycling after adsorption [25–27]. Moreover, Fe_3O_4 shows excellent separate characteristics due to its magnetic properties [28]. Therefore, it has been widely used in wastewater treatment in recent years [29–31]. In previous studies, Sun et al. [32] prepared Fe_3O_4 @C submicron rods by hydrothermal carbonization to remove MB in aqueous solution, but the larger particle size affects the comparison area and reduces the adsorption efficiency of MB. Rsjput et al. [33] synthesized Fe_3O_4 nanoparticles by co-precipitation to adsorb Pb^{2+} . However, Fe_3O_4 nanoparticles are easy to agglomerate and the maximum adsorption capacity is only 53.11 mg/g. Therefore, it is necessary to study and prepare an adsorbent that can prevent Fe_3O_4 nanoparticles from agglomerating and has good pollutant removal effect.

Metal–organic framework materials (MOFs) based on their huge porosity, large specific surface area, adjustable pore size, etc. [34,35], are very broad prospects for various applications [36]. In recent years, various MOF materials have been applied to wastewater treatment. Abdi et al. [37] reported zeolite imidazolate framework (ZIF-8) nanocomposites prepared with graphene oxide (GO) and carbon nanotubes (CNT) as substrates to remove malachite green (MG) from colored wastewater. Lin et al. [38] synthesized a zirconium-based MOF (UiO-66- NH_2) to remove fluoride in wastewater and the crystal structure of UiO-66- NH_2 remained intact during the adsorption process. Efome et al. [39] synthesized water-based metal organic framework particles (Zr-808) on the surface of polyacrylonitrile (PAN) nanofibers, and the maximum adsorption capacities for heavy metal ions (Cd^{2+} and Zn^{2+}) in aqueous solution were 225.05 and 287.06 mg/g, respectively. Although the MOF material can effectively remove pollutants in water, it is difficult to separate and recover quickly at the end of adsorption, which limits its practical application in wastewater treatment. In our work, fibers were extracted from durian shell and Fe_3O_4 nanoparticles were loaded onto its surface, which not only realized the resource reuse of durian shell, but also effectively reduced the agglomeration of Fe_3O_4 nanoparticles. At the same time, the combination of Fe_3O_4 nanoparticles and MOF materials can effectively solve the problem that MOF materials are difficult to separate from aqueous solution. In this paper, the durian shell fiber- Fe_3O_4 MOF composite was synthesized by a step-by-step method to remove methylene blue (MB) from wastewater. The structures were characterized by SEM, TEM, XRD, and XPS techniques. The effects of adsorption time, initial concentration, temperature, and pH value on the adsorption process, and the adsorption kinetics, isotherm, and thermodynamics of MB were studied.

2. Results and Discussion

2.1. SEM and TEM Analysis

The morphology and structure of DF, DFM-10, DFM-20, and DFM-40 samples at different magnifications were observed by SEM and TEM and the result are shown in Figures 1, 2 and S1. The width of durian shell fiber was around 10 μm and the surface of durian shell fiber was relatively smooth (Figure S1). As can be seen from DF images, the particle size of Fe_3O_4 was uniform and the magnetic Fe_3O_4 nanoparticles were successfully loaded onto the surface of durian shell fibers. From SEM results of DFM-10, DFM-20, and DFM-40, the magnetic Fe_3O_4 nanoparticles were successfully wrapped with a layer of MOF shell. After 10 cycles, sample DFM-10 showed a rough surface. The thickness of the MOF shell gradually increased with the increase in cycle numbers. However, after 20 and 40 cycles, the thickness of the MOF shell had a very significant increase compared with that after 10 cycles and the magnetic Fe_3O_4 nanoparticles appeared cross-linked and agglomerated. From TEM images, we found that the Fe_3O_4 nanoparticles were surrounded by MOF shells. As the number of cycles increased, the thickness of the MOF shell gradually increased.

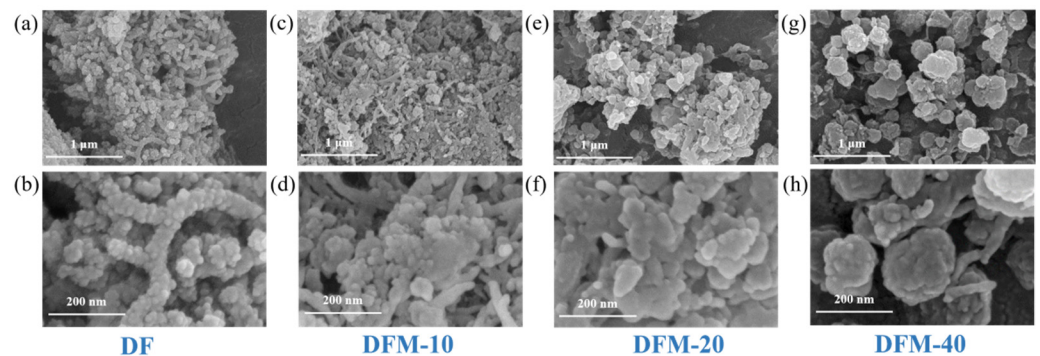


Figure 1. SEM images of DF (a,b), DFM-10 (c,d), DFM-20 (e,f), and DFM-40, and (g,h) samples at different magnifications.

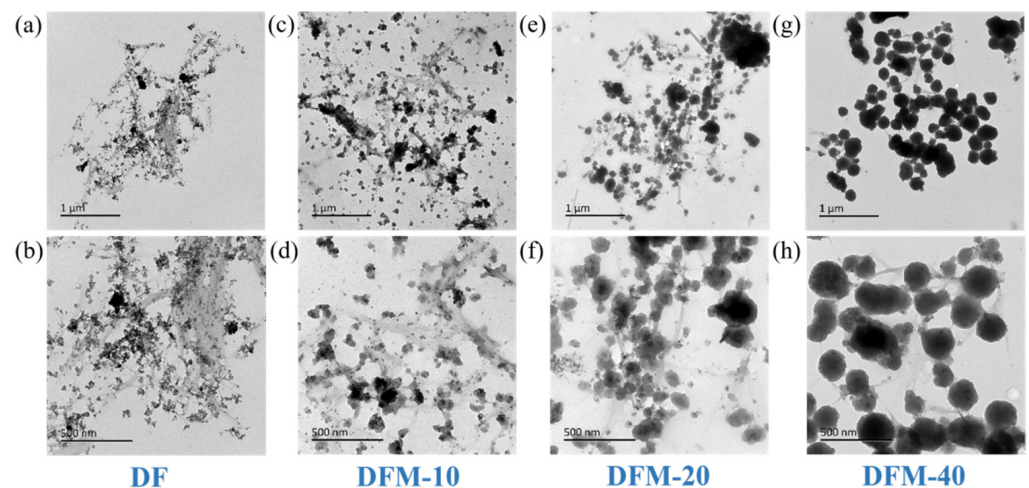


Figure 2. TEM images of DF (a,b), DFM-10 (c,d), DFM-20 (e,f), and DFM-40, and (g,h) samples at different magnifications.

The XRD peaks of the durian shell fiber and the prepared DF, DFM-10, DFM-20, and DFM-40 are shown in Figure 3a. As can be seen from (A), the crystal lattice of the durian shell fibers had peaks of 15.9° and 21.88° , which is consistent with previous literature reports [40]. The X-ray diffraction pattern of DF in (B) shows the result of diffraction peaks at 2θ values of 30.1° (220), 35.5° (311), 43.2° (400), 57.1° (511), and 62.8° (440), which is consistent with the standard XRD (JCPDS card, file No. 89-4319) data of Fe_3O_4 with a face-centered cubic structure reported in [41]. DFM-10, DFM-20, and DFM-40 also had the same diffraction peaks (C–E), indicating that the lattice structure of Fe_3O_4 will not be destroyed after many cycles. At the same time, with the loading of Fe_3O_4 and the MOF structure of the synthetic durian shell fiber, the diffraction peaks at 13° to 25° were significantly weakened. FTIR spectra of durian shell fiber (A), DF (B), and DFM-10 (C) materials are shown in Figure 3b. The peaks at 560 and 630 cm^{-1} could be ascribed to the stretching vibration of Fe–O in Fe_3O_4 , indicating the existence of Fe_3O_4 in the materials. Additionally, peaks at 1634 and 1421 cm^{-1} were observed in the products of DFM-10, which, respectively, corresponded to C=C and C–O vibrations, confirming the presence of carboxylate groups. The carboxylate group in H_3BTC combines with Fe^{3+} ions to coordinate to form MOF. In this way, the growth of MOF shell proceeded on the DF. The vibration bands corresponded to the –O–C–O– groups around 1574 cm^{-1} and 1384 cm^{-1} , indicating the presence of the dicarboxylate within the compound. The strong stretching-vibration bands in the range of $3050\text{--}3500\text{ cm}^{-1}$ belonged to –OH and – NH_2 .

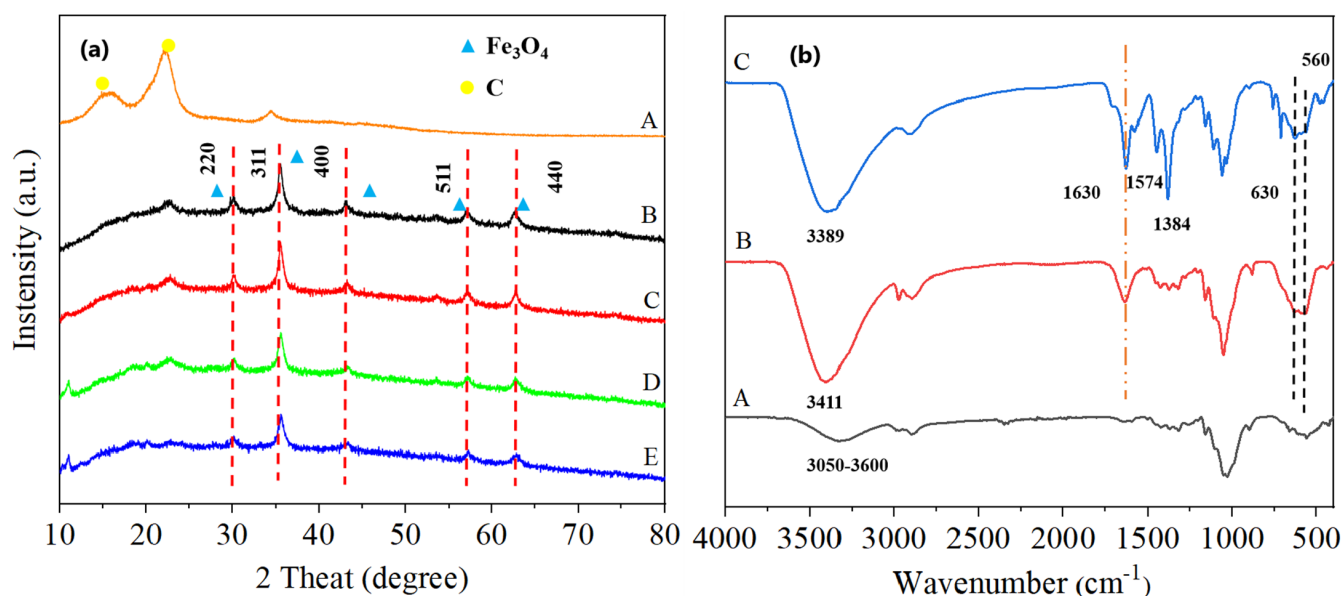


Figure 3. (a) XRD patterns of durian shell fiber (A), DF (B), DFM-10 (C), DFM-20 (D), and DFM-40 (E) and (b) FTIR spectra of durian shell fiber (A), DF (B), and DFM-10 (C).

XPS was used to observe the changes in the chemical valence state of the elements before and after the adsorption of MB by DFM-10, and the spectra of C 1s, O 1s, Fe 2p, and broad scans are showed in Figure 4. Figure 4a shows the C 1s spectrum, which had three main peaks, namely C–C (284.8 eV), C–O–C (268.1 eV), and O–C=O (287.7 eV). Figure 4b shows the O 1s spectrum. The peak value was at 532.64 eV binding energy and the peak value did not change before and after adsorption, indicating that no oxidation–reduction reaction was involved in the adsorption process. Figure 4c shows the spectrum of Fe 2p. It can be seen that the peaks at 711.05 eV and 724.85 eV represent $\text{Fe}2p_{3/2}$ and $\text{Fe}2p_{1/2}$, respectively, which indicates that Fe^{2+} and Fe^{3+} co-exist in the synthesized DFM-10. The total distribution energy spectrum of each element is shown in Figure 4d, from which it can be seen that there was little change before and after adsorption, indicating that the synthesized DFM-10 is a stable material. there was no obvious change in the characteristic

peaks of the material before and after adsorption (A and B), indicating that DFM-10 was a stable material.

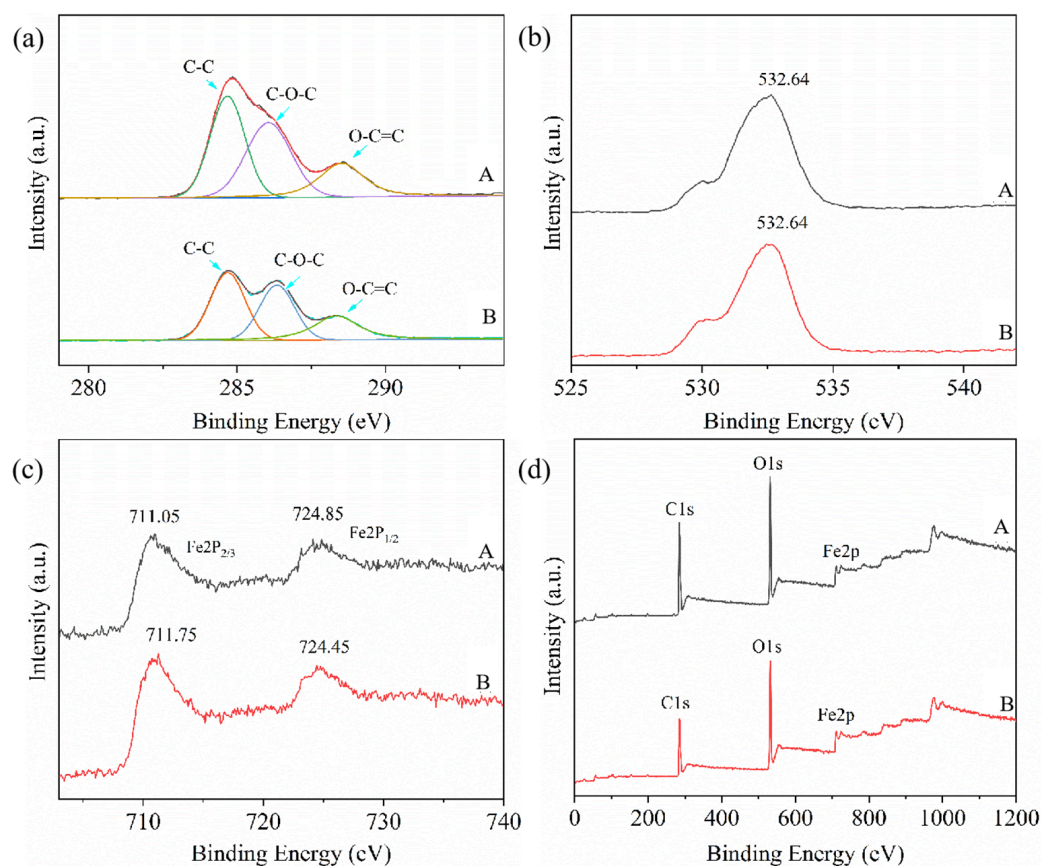


Figure 4. XPS spectra of C 1s (a), O 1s (b), Fe 2p (c), and broad scans (d) of DFM-10 before (A) and after (B) the adsorption of MB.

2.2. Adsorption Experiments

2.2.1. Effect of Different Concentrations

To select a more suitable adsorbent, the adsorption performance of DF, DFM-10, DFM-20, and DFM-40 were evaluated. The adsorbent (5 mg) was mixed with MB solutions of different initial concentrations (5 mg/L, 10 mg/L, and 15 mg/L), and placed in constant-temperature oscillator at 25 °C. After a reaction time of 3 h, the adsorbent material was collected with a magnet. As shown in Figure 5, compared with DFM-0, the adsorption capacities of DFM-10, DFM-20, and DFM-40 were significantly improved, indicating that the introduction of a MOF structure significantly improve the adsorption performance of the material. The adsorption capacities of DFM-10 and DFM-20 to different concentrations of MB were basically the same, but the adsorption capacity of DFM-40 to MB was slightly lower than those of DFM-10 and DFM-20. Combined with SEM and TEM characterization, the reason may be that as the number of cycles increased, the thickness of the MOF shell gradually increased, and the MOF shell outside the adjacent magnetic Fe₃O₄ nanoparticles underwent crosslinking and agglomeration, which prevented the MB molecules from diffusing into the material, resulting in a decrease in adsorption effect. Therefore, DFM-10 was selected as the adsorbent, and its adsorption isotherm model, adsorption kinetics, and adsorption thermodynamics for MB were studied.

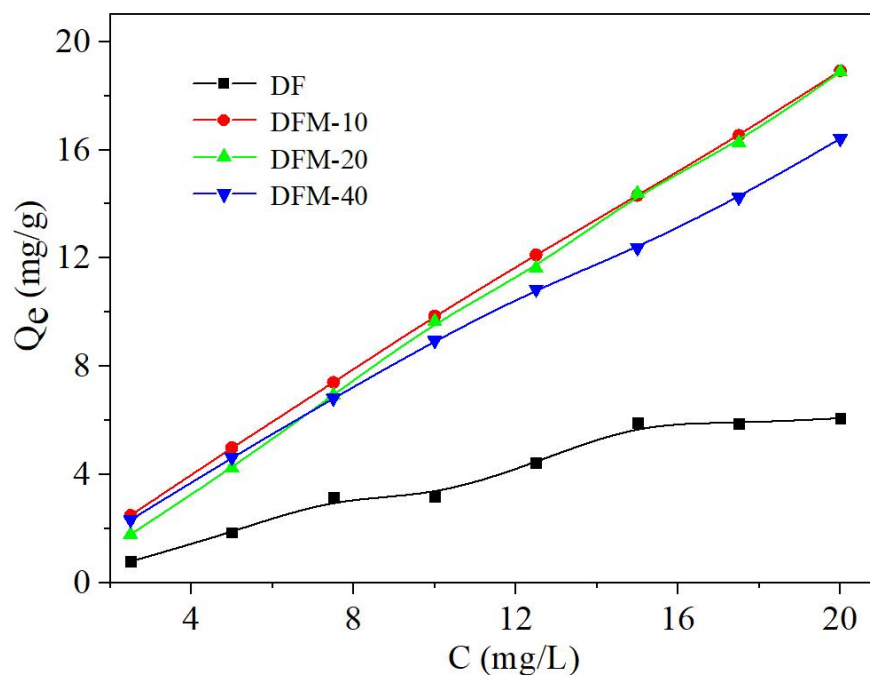


Figure 5. Adsorption effects of DF, DFM-10, DFM-20, and DFM-40 on MB at different concentrations.

2.2.2. Effect of pH and Ionic Strength

pH plays a significant role in the process of adsorption. Therefore, the adsorption capacity of DF, DFM-10, DFM-20, and DFM-40 under different pH was studied, and the results can be seen in Figure 6a. It can be seen from the figure that as the pH value rose from 2 to 12, the adsorption capacity of DFM-0 on MB gradually increased. This was because of the presence of a large amount of H^+ in the particles at low pH solutions, which led to the protonation of the Fe_3O_4 nanoparticle surface. However, the MB molecule was positively charged, so electrostatic repulsion occurred between the two, resulting in a small amount of adsorption. With the gradual increase of pH, the surface of nano- Fe_3O_4 gradually deprotonated, so the adsorption capacity of MB gradually increased. However, the adsorption amount of MB on DFM-10, DFM-20, and DFM-40 did not change significantly with the increase of pH. This shows that the electrostatic interaction between DFM-10 (or DFM-20, DFM-40) and MB during the adsorption process was not the main factor affecting the adsorption effect. The larger adsorption capacity of DFM-10, DFM-20, or DFM-40 on MB may be attributed to the porous structure of the adsorbent itself, the van der Waals force and hydrogen bonding between the -OH and -COOH groups on the surface of DFM-10 (or DFM-20, DFM-40) and the MB molecule. Studying the influence of pH on the adsorption capacity provides an important reference for the practical application of materials. Therefore, considering comprehensive considerations, pH = 9 was selected in the next experiment. As can be seen from Figure 6b, the isoelectric point (pHpzc) of DFM-10 was at 5.9, suggesting that the surfaces of the prepared DFM-10 adsorbents were positively charged at pH < 5.9 and the negatively charged at pH > 5.9.

In this work, NaCl and $CaCl_2$, two common salts, were selected to judge the effects of ionic strength on the process of MB adsorption on DFM-10. As shown in Figure 6c, with the increase of salt concentration from 0 to 0.1 mol/L, the adsorption capacity decreased initially. This is because ionic strength reduced the surface charge of DFM-10 and MB, resulting in the decrease of adsorption capacity. When the concentration increased from 0.1 to 0.3 mol/L, the adsorption capacity increased because the salt may have reduced the solubility of MB in water. The decrease of solubility promoted the diffusion of more MB molecules to the adsorbent surface, thus improving the adsorption capacity. When the concentration of NaCl and $CaCl_2$ was at 0.3 mol/L, these two salts showed the same effect on adsorption capacity. From 0.3 mol/L to 0.5 mol/L, the adsorption capacity showed a

slight fluctuation. Although the adsorption capacity was reduced, the reduction was only 23.12%. Therefore, the results showed that the prepared DFM-10 adsorbent had potential application prospects in the treatment of wastewater containing MB.

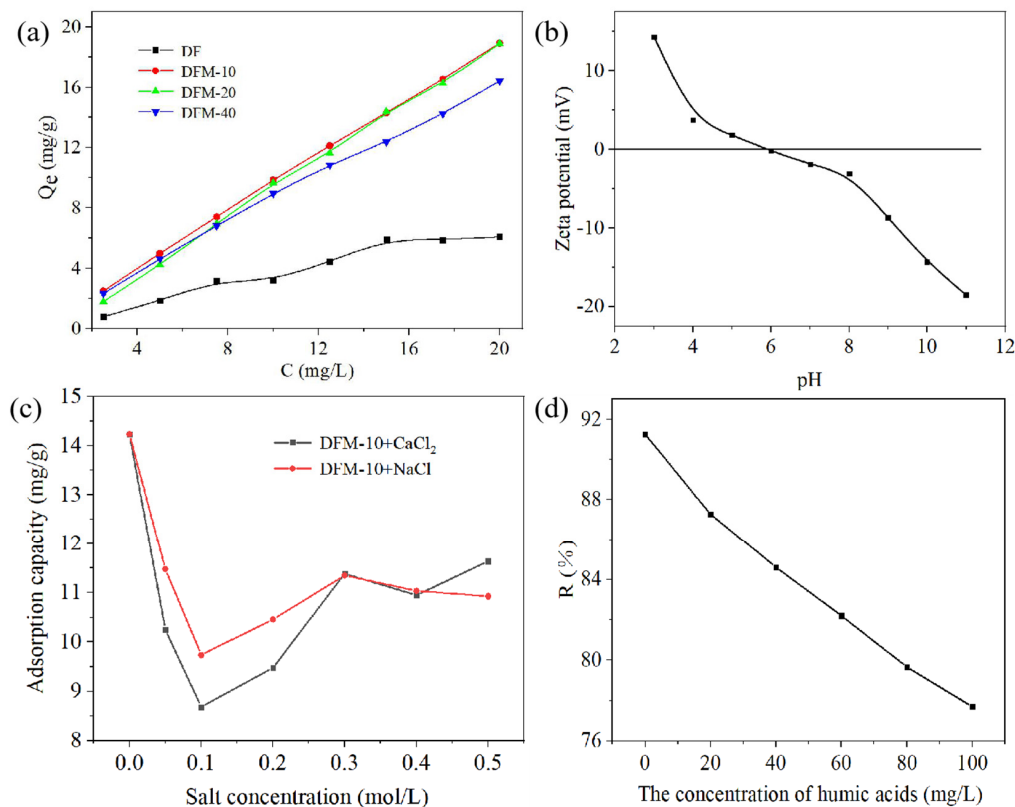


Figure 6. (a) Adsorption effects of DF, DFM-10, DFM-20, and DFM-40 on MB at different pH values, (b) zeta potential of DFM-10 adsorbent, (c) effect of ionic strength on the adsorption capacity, and (d) effects of humic acids solution concentration on MB removal percent.

The competitor experiments were performed towards humic acids under the optimal adsorption condition (adsorbent dosage: 5 mg; initial concentration of MB: 20 mg/L (10 mL); pH: 6; temperature: 25 °C; adsorption time: 3 h), and the results were shown in Figure 6d. As can be seen from Figure 6d, with increasing concentration of humic acids, the MB removal percent decreased. This could have been the result of the competitive effect between humic acids and MB molecule by electrostatic adsorption. However, the MB removal percent decreased by only 18.09% although the concentration of 100 mg/L for humic acids was far higher than that in a realistic water environment, indicating that the adsorbents have the potential to be employed for MB adsorption.

2.2.3. Effect of Time and Initial Concentration of MB

We added 5 mg of adsorbent to 15 mL of MB solution at concentrations of 5 mg/L, 10 mg/L, and 15 mg/L, and, after ultrasonic dispersion, placed the solutions in a constant-temperature shaker at 25 °C and vibrated for adsorption. The effects of different initial concentrations and adsorption time on the adsorption performance of DFM-10 were studied with time-interval sampling, and the results are shown in Figure 7.

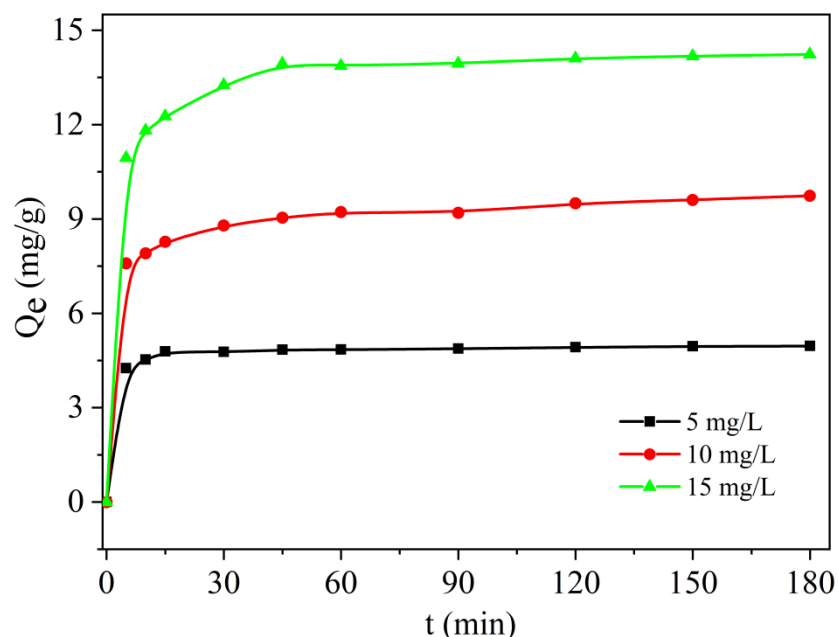


Figure 7. The relationship between adsorption amount and time of MB adsorbed by DFM-10 at different concentrations.

It can be seen that with the increase of initial concentration, the adsorption amount of MB by DFM-10 also gradually increased. The adsorption process of MB on DFM-10 can be divided into two stages. The first stage was within 0–15 min after the beginning of adsorption. When the adsorbent is added, MB molecules quickly combined with the adsorption sites on the surface of DFM-10, and the adsorption capacity increased rapidly. With the passage of time, the adsorption sites were gradually occupied, which slowed down the diffusion rate of MB molecules into the adsorbent. Therefore, the increase of adsorption amount gradually slowed until the adsorption sites were completely occupied, an adsorption saturation state was reached, and the adsorption amount did not increase.

2.3. Adsorption Isotherms

To study the adsorption performance of DFM-10 to MB and their interaction pathways, Langmuir, Freundlich, Temkin, and Dubinin–Radushkevich adsorption isotherm models were used. [42]. The Langmuir isotherm model assumes that only a single layer of adsorption occurs on the limited active sites on the surface of the adsorbent, and there is no interaction between adjacent sites [43]. The Freundlich isotherm model assumes that the adsorption process is a multilayer adsorption, and there are interactions between adsorbate molecules [44]. The Temkin isotherm model considers the interaction between adsorbate and adsorbent. The Temkin model assumes that the adsorption heat of all molecules in the layer will decrease linearly with the accumulation of adsorbed molecules on the adsorbent surface. The Dubinin–Radushkevich isotherm model is an empirical model initially conceived for the adsorption onto micropore solids following a pore-filling mechanism. It is generally applied to express the adsorption mechanism with a Gaussian energy distribution onto a heterogeneous surface [21].

The Langmuir, Freundlich, Temkin, and Dubinin–Radushkevich isotherm models are represented by the following equations:

$$\text{The Langmuir isotherm model equation : } \frac{C_e}{Q_e} = \frac{1}{Q_L K_L} + \frac{C_e}{Q_L} \quad (1)$$

$$\text{The Freundlich isotherm model equation : } \ln Q_e = \ln K_F + \frac{1}{n} \ln C_e \quad (2)$$

$$\text{The Temkin isotherm model equation : } Q_e = \left(\frac{RT}{b_T}\right) \ln K_T + \left(\frac{RT}{b_T}\right) \ln C_e \quad (3)$$

$$\text{The Dubinin–Radushkevich isotherm model equation : } \ln Q_e = \ln Q_m - K_{DR}\epsilon^2 \quad (4)$$

$$\epsilon = RT \ln \left[1 + \frac{1}{C_e} \right] \quad (5)$$

where Q_e (mg/g) shows the adsorption capacity at equilibrium and Q_L (mg/g) is the theoretical maximum adsorption capacity. C_e (mg/L) represents the concentration when the adsorption equilibrium is reached and K_L is the Langmuir constant (L/mg). K_F is the Freundlich constant ($\text{mg}^{1-1/n} \cdot \text{L}^{1/n}/\text{g}$). $1/n$ is the parameter characterizing the energy heterogeneity of the adsorption surface. b_T is the Temkin constant related to heat of adsorption (J·g/mol·mg). K_T is the Temkin isotherm equilibrium binding-energy constant (L/mg). R is the gas constant (8.314 J/mol·K). T is the absolute temperature (K). K_{DR} is the constant related to the adsorption energy ($\text{mol}^2 \cdot \text{J}^2$). ϵ is the adsorption potential (J/mol) [45,46].

The Langmuir, Freundlich, Temkin, and Dubinin–Radushkevich isotherm models of MB adsorption by DFM-10 at different temperatures (298 K, 308 K, and 318 K) are shown in Figure 8, and the corresponding fitting parameters are listed in Table 1. It can be seen that the R^2 of the Langmuir isotherm fitting model was in the range 0.9791–0.9948, and the fitting curves was basically consistent with the experimental plots. The R^2 of Freundlich, Temkin, and Dubinin–Radushkevich isotherm models were in the ranges 0.9570–0.9766, 0.8447–0.8910, and 0.8567–0.8811, respectively, and the fitting curves were inconsistent with the experimental data. The correlation coefficients of the isotherms were in the order Langmuir > Freundlich > Temkin > Dubinin–Radushkevich. The above results indicate that the Langmuir isotherm model was more appropriate for fitting the experimental data than other three models. In addition, with the increase of temperature, the adsorption amount also gradually increased, indicating that heating was conducive to the adsorption process. Monomolecular layer adsorption could have played a vital role, and the maximum adsorption capacities were 53.31 mg/g at temperature of 318 K. In the case of the Freundlich isotherm model, the constant of Freundlich adsorption (K_F) increased with increasing adsorption temperatures. High values of K_F indicated that there was very good interaction between DFM-10 and MB.

Table 1. Langmuir, Freundlich, Temkin, and Dubinin–Radushkevich adsorption isotherm model parameters.

Model	Parameter	298 K	308 K	318 K
Langmuir	Q_L (mg/g)	34.8100	42.2500	53.3100
	K_L (L/mg)	1.8427	1.3402	1.9642
	R^2	0.9931	0.9948	0.9791
Freundlich	K_F ($\text{mg}^{1-1/n} \text{L}^{1/n} / \text{g}$)	20.5600	22.6900	30.6800
	$1/n$	0.2065	0.2624	0.2862
	R^2	0.9766	0.9609	0.9570
Temkin	b_T (J·g/mol·mg)	0.7053	0.5124	0.4142
	K_T (L/mg)	1.0065	1.0051	1.0054
	R^2	0.8910	0.8735	0.8447
Dubinin–Radushkevich	Q_L (mg/g)	28.3731	31.8753	40.1395
	K_{DR} (mol ²)	0.1105	0.1432	0.1423
	R^2	0.8802	0.8567	0.8811

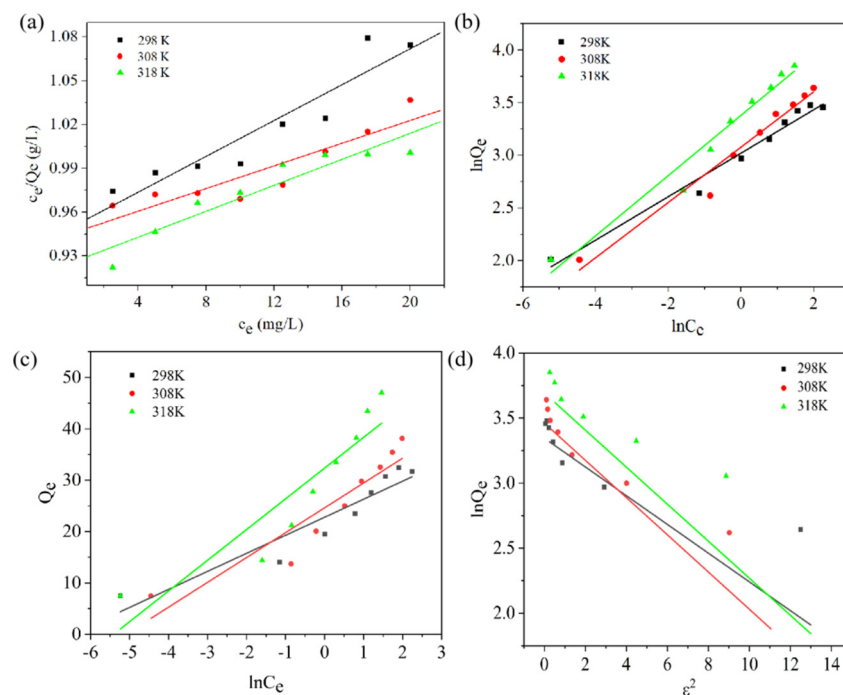


Figure 8. Langmuir (a), Freundlich (b), Temkin (c), and Dubinin–Radushkevich (d) isotherms of MB adsorption on DFM-10.

2.4. Adsorption Kinetics

To calculate the adsorption kinetics of DFM-10 adsorbing MB, the experimental data were analyzed through pseudo-first-order, pseudo-second-order, and intraparticle diffusion kinetic models. The pseudo-first-order, pseudo-second-order, and intraparticle diffusion kinetic models are expressed by the following equations [47]:

$$\ln(Q_e - Q_t) = \ln Q_e - K_1 t \quad (6)$$

$$\frac{t}{Q_t} = \frac{1}{K_2 Q_e^2} + \frac{t}{Q_e} \quad (7)$$

$$Q_t = K_p t^{1/2} + C \quad (8)$$

where Q_e is adsorbed by adsorbents at equilibrium and Q_t (mg/g) is the amount of MB adsorbed at time t . K_1 (min^{-1}), K_2 ($\text{g mg}^{-1} \text{min}^{-1}$), and K_p ($\text{mg g}^{-1} \text{min}^{1/2}$) are the rate constants of adsorption for the pseudo-first-order, pseudo-second-order, and intraparticle diffusion kinetic models.

Under the same temperature and dosage, different concentrations (5, 10, and 15 mg/L) of MB solution were selected to study the adsorption effect of DFM-10 on MB at different times. The fitting curves of pseudo-first-order (a), pseudo-second-order (b), and intraparticle diffusion (c) kinetic models of MB were obtained by data analysis and fitting as shown in Figure 9, and the corresponding fitting parameters are listed in Table 2. It can be seen from the fitting results that at different concentrations, the R^2 (0.9998, 0.9998, 0.9998) of the pseudo-second-order kinetic fitting model of DMF-10 for MB adsorption was greater than that of the pseudo-first-order kinetic fitting model (0.6817, 0.8401, 0.9523) and intraparticle diffusion kinetic model. This indicates that the adsorption process of DMF-10 to MB is more complex in the pseudo-second-order kinetic model, and the adsorption process is dominated by chemical adsorption. With the increase of initial concentration, the rate constant K_2 of the pseudo-second-order kinetic model decreased gradually. This shows that with the increase of initial dye concentration, the adsorption rate gradually slowed down, and the adsorption rate was faster at low concentration. The intraparticle diffusion kinetic curves were treated to test whether internal particle diffusion or external diffusion was

the rate-limiting step. The intraparticle diffusion kinetic plot did not match the origin of coordinates (Figure 9c). This result indicated that the adsorption mechanism was influenced by multi-mechanisms, and that internal particle diffusion may be not the main element.

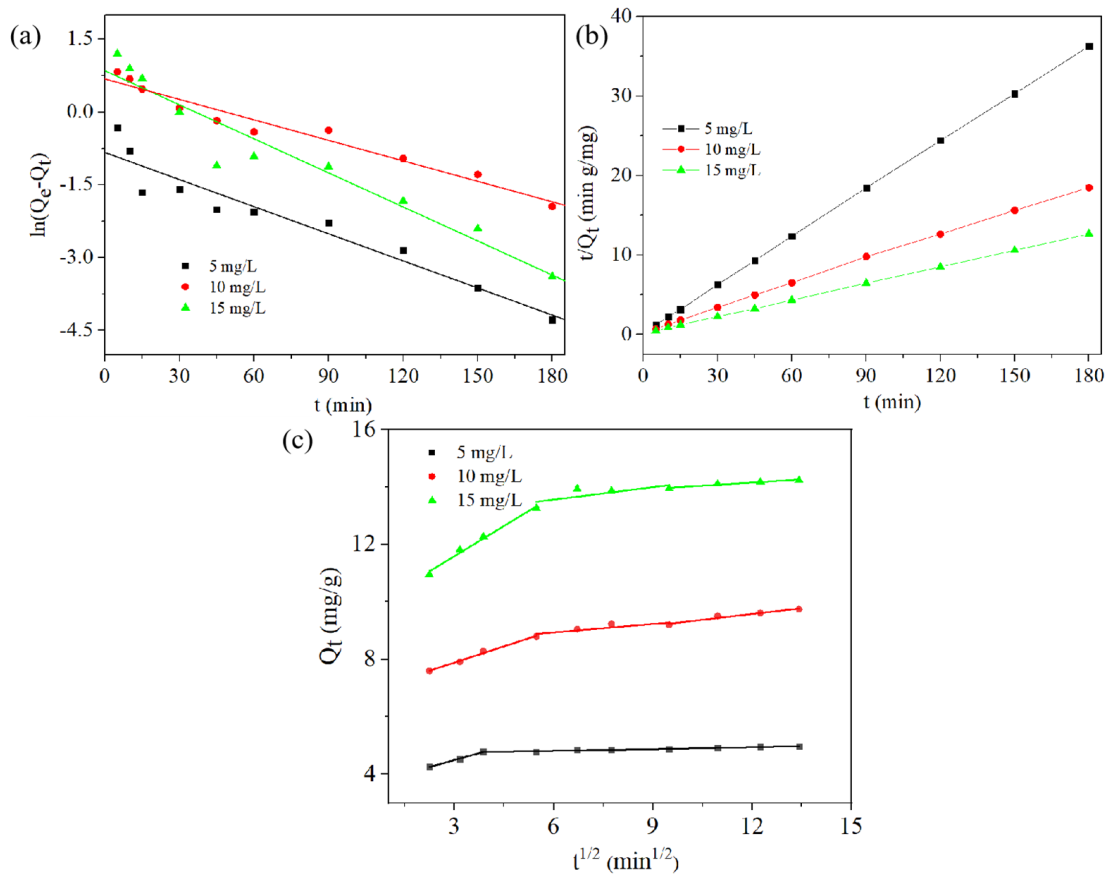


Figure 9. Pseudo-first-order (a), pseudo-second-order (b), and intraparticle diffusion (c) kinetic models fitting curves of MB.

Table 2. Pseudo-first-order, pseudo-second-order, and intraparticle diffusion dynamics-model-related parameters.

Model	Parameter	5 (mg/L)	10 (mg/L)	15 (mg/L)
Pseudo-first-order	Q_e (mg/g)	1.5100	4.0900	6.8100
	K_1 (/min)	0.0225	0.0301	0.0438
	R^2	0.6817	0.8041	0.9523
Pseudo-second-order	Q_e (mg/g)	15.0900	27.6000	37.5100
	K_2 (g/(mg min))	0.0581	0.0171	0.0101
	R^2	0.9998	0.9998	0.9998
	K_{p1} (mg/g/min ^{1/2})	0.3237	0.3767	0.7017
	C_1 (mg/g)	3.5209	6.7550	9.4854
Intraparticle diffusion	R^2	0.9961	0.9928	0.9884
	K_{p2} (mg/g/min ^{1/2})	0.0184	0.0993	0.1144
	C_2 (mg/g)	4.7022	8.3343	12.6905
	R^2	0.8202	0.7468	0.5608
	K_{p3} (mg/g/min ^{1/2})	0.0230	0.1345	0.0730
	C_3 (mg/g)	4.6616	7.9615	13.2741
	R^2	0.9665	0.9591	0.9548

2.5. Thermodynamic Study

In order to understand the effect of temperature on the adsorption of MB by DFM-10 and affirm the adsorption process, thermodynamic results from the adsorption data of MB were calculated at three different temperatures by using DFM-10 (298 K, 308 K, and 318 K): Gibbs free energy ΔG (KJ/mol), enthalpy change ΔH (KJ/mol) and entropy change ΔS (J/(mol·K)) [48]. The calculation formula of each thermodynamic parameter is as follows:

$$K_e = \frac{Q_e}{C_e} \quad (9)$$

$$\Delta G = -RT \ln K_e \quad (10)$$

$$\ln K_e = \frac{\Delta S}{R} - \frac{\Delta H}{RT} \quad (11)$$

where R is the ideal gas constant ($8.314 \text{ J/mol}^{-1} \text{ K}^{-1}$). T acted as the absolute temperature (K). K_e is the thermodynamic equilibrium constant, Q_e (mg/g) is the amount of adsorption at adsorption equilibrium, and C_e (mg/L) is the equilibrium concentration [49]. We plotted $\ln K_e$ versus $1/T$ and calculated ΔS from the intercept and ΔH from the slope. The calculation results are listed in Table 3.

Table 3. Thermodynamic parameters for MB adsorption by DFM-10.

ΔH (KJ/mol)	ΔS (J/(mol·K))	ΔG (kJ/mol)			R^2
		298 K	308 K	318 K	
4.6747	16.8786	−3.0115	−4.2291	−5.8263	0.9851

It can be seen from Table 4 that ΔH was positive, indicating that the adsorption of MB in aqueous solution by DFM-10 was an endothermic process. The higher the temperature, the better the adsorption effect. When ΔH was less than 40 kJ/mol, the adsorption process was dominated by physical adsorption [50], and the ΔH value of the adsorption of MB in aqueous solution by DFM-10 was 4.6747 kJ/mol within this range, indicating that the adsorption process was dominated by physical adsorption. ΔG was negative, indicating that the adsorption process of DFM-10 to MB was spontaneous, and as the temperature increased, the value of ΔG gradually decreased, which shows that the spontaneity of the reaction was gradually increasing as the temperature rose. When the value of ΔG is in the range of -20 to 0 kJ/mol, the adsorption process is physical adsorption. Obviously, the ΔG value of the adsorption of MB in the aqueous solution by DFM-10 was within this range, indicating that the adsorption process was physical adsorption, which is consistent with the discussion of the ΔH value. In addition, ΔS was 16.8767 kJ/mol greater than 0, indicating that the disorder of the solid–liquid interface increased during the process of adsorption and the adsorption process was irreversible. Thermodynamic studies have shown that the adsorption of MB in aqueous solution by DFM-10 is a spontaneous endothermic physical adsorption process.

Table 4. Porous performance parameters of DF and DFM-10.

Samples	DF	DFM-10
Mean pore radius (nm)	10.53	5.45
Total pore volume ($\text{cm}^3 \text{ g}^{-1}$)	0.19	0.24
BET surface area ($\text{m}^2 \text{ g}^{-1}$)	60.55	226.88

Based on all the discussions above, the interaction mechanism when DFM-10 adsorbs MB is proposed, as shown in Figure 10. It can be seen from Table 4 that the specific surface area of DFM-10 is $226.88 \text{ m}^2/\text{g}$, which is significantly higher than that of DFM-10. At the same time, DFM-10 has smaller mean pore radius and larger total pore volume, which provides a good structural basis for MB adsorption. Meanwhile, in the metal–organic framework (MOF) synthesis process, H_3BTC and MB molecules have a weak interaction and can be adsorbed by hydrogen bonds and other forces [51]. The $-\text{OH}$ structure in DFM-10 can be used as a π electron donor, and the conjugated unsaturated carbonyl structure in MB molecule can be used as a π electron acceptor. Therefore, the π – π interaction in the adsorption process may be a potential mechanism.

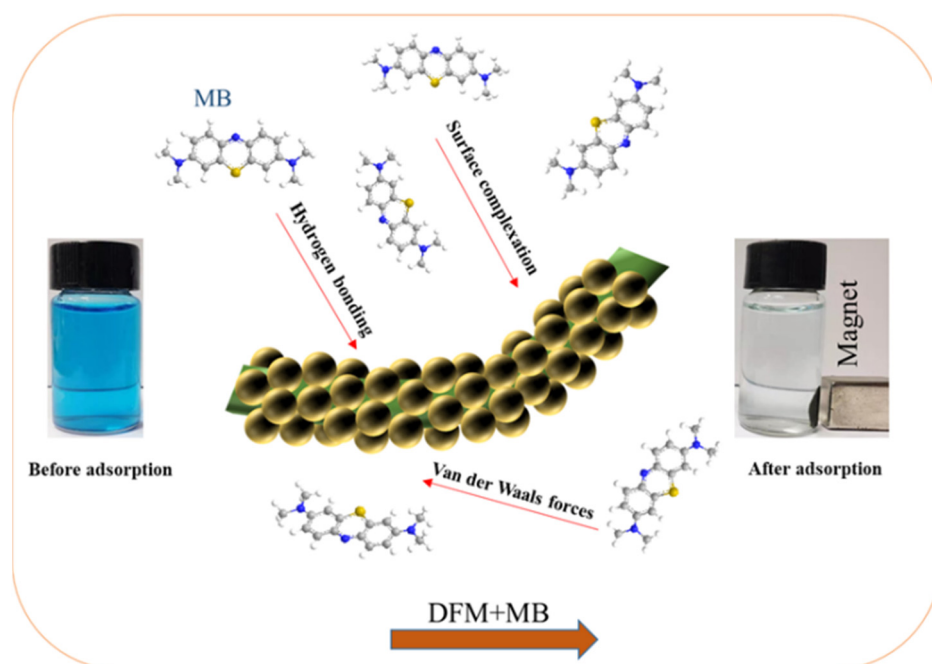


Figure 10. Possible adsorption mechanism of MB onto DFM-10.

Figure 11 shows the separation performance of DFM-10 in aqueous solution. It can be seen from the same figure that under the action of a strong magnet, DFM-10 can be basically separated from aqueous solution within 9 s, and can be completely separated from aqueous solution within 30 s. This is because the load of Fe_3O_4 provides the ability for rapid separation of DFM-10 from aqueous solution.

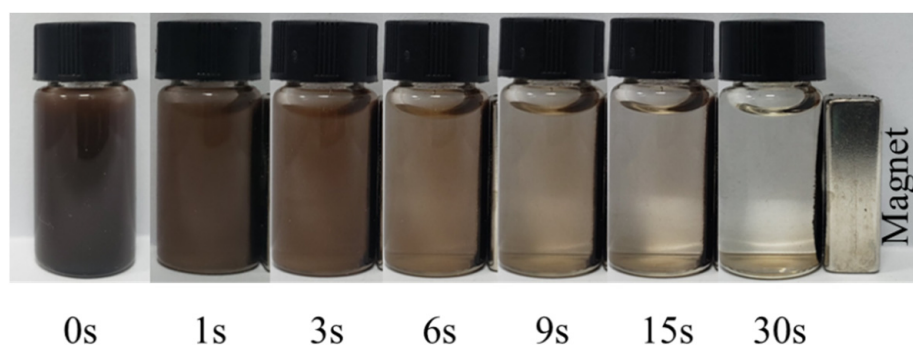


Figure 11. Magnetic separation process of DFM-10 in solution.

2.6. Total Organic Carbon (TOC) Analysis

The total organic carbon (TOC) is an indicator for evaluating the removal of organic pollutants in water. Figure 12 showed the TOC amount of the natural river water (Hung-tse Lake in Jiangsu Province, Hongze) before and after adsorption by DFM-10. The initial amount of TOC was 51.22 mg/L before adding DFM-10. After the adsorption reaction, the TOC amount decreased to 4.39 mg/L. The results indicated that the TOC removal rate reached 91.44%, indicating that the adsorbent had excellent purification performance.

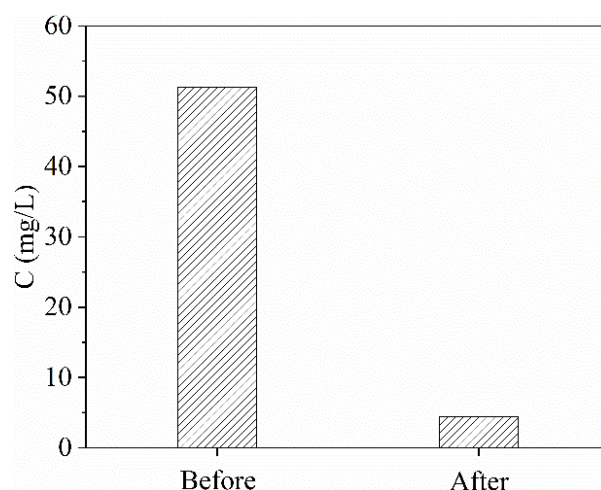


Figure 12. Removal effect of DFM-10 on TOC in actual wastewater.

2.7. Recycling Ability

Through cyclic experiments, we studied whether DFM-10 can be recycled, which has an important impact on the practicality of the adsorbent. We conducted MB adsorption-cycle experiments on DFM-10 five times. At 298 K, the initial concentration of MB was 10 mg/L. After 3 h of adsorption, the adsorption was carried out with HCl/ethanol (0.5%, v/v). The obtained result is shown in Figure 13. It can be seen from Figure 13a that the removal rate of MB by DFM-10 was 90.50% in the first cycle. After five cycles, the removal rate of MB by DFM-10 remained at 83.15% without significant decrease. From Figure 13b, the crystal structure of DFM-10 had no apparent change after four consecutive cycle reactions, suggesting that DFM-10 could be used as an efficient and recyclable adsorbent to remove MB from wastewater. The removal efficiency of DFM-10 for MB was also higher than reported adsorbents, as mentioned in Table S1 [52–57].

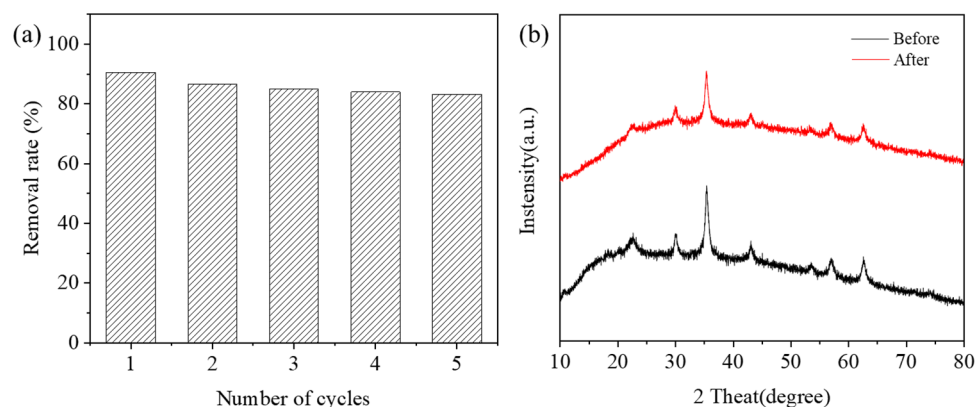


Figure 13. (a) Recycling performance of DFM-10 adsorbent and (b) XRD patterns of DFM-10 before and after five reaction cycles.

3. Materials and Methods

3.1. Chemicals and Reagents

Durian shells were purchased from supermarket in Nanjing. Ferric chloride hexahydrate ($\text{FeCl}_3 \cdot 6\text{H}_2\text{O}$) and sodium chlorite (NaClO_2) were from Shanghai Macklin Biochemical Co., Ltd. (Shanghai, China) Benzene-1, 3, 5-tricarboxylic acid (H_3BTC) and urea ($\text{CH}_4\text{N}_2\text{O}$) were purchased from Aladdin Reagent Co., Ltd. (Shanghai, China). Sodium hydroxide (NaOH), sodium bicarbonate (NaHCO_3), and methylene blue (MB) were purchased from Sinopharm Chemical Reagent Co., Ltd. (Shanghai, China). Vitamin C ($\text{C}_6\text{H}_8\text{O}_6$) was purchased from Yuanye Biological Technology Co., Ltd. (Shanghai, China). All the above chemical reagents were used without further purification.

3.2. Synthesis of Adsorbent

3.2.1. Extraction of Durian Shell Fiber

Firstly, 25 g of durian shell was dried at 60°C for 6 h, cut into pieces, and placed in a NaOH solution (1 M, 500 mL). The solid was then stirred at 85°C for 4 h to remove cellulose and impurities. Subsequently, the durian shell fibers were put into a 5 wt% NaClO_2 solution for decolorization, and magnetically stirred at 80°C for 2h, filtered, separated, washed five times with deionized water, and dried at 60°C for 24 h to get durian shell fibers.

3.2.2. Preparation of Durian Shell Fiber- Fe_3O_4 (DF)

Firstly, 0.2 g durian husk fiber, 2.0 g NaOH , and 4.0 g $\text{CH}_4\text{N}_2\text{O}$ were dissolved in 40 mL deionized water, stirred to form a transparent solution, and flocculent fibers were collected. Secondly, 0.2 mol/L $\text{FeCl}_3 \cdot 6\text{H}_2\text{O}$ solution (10 mL) was added to 0.45 mol/L NaHCO_3 solution (10 mL), and then vigorously stirred for 30 min. Then, 0.03 mol/L vitamin C solution (10 mL) was added to above-mentioned flocculent durian shell fiber and stirred for 20 min at 25°C . Then, the material was put into a 50 mL Teflon kettle and heated at 180°C for 8 h. The final products could then be separated with ethanol and washed with deionized water three times, collected by centrifugation (8000 rpm) and dried at 80°C for 12 h to obtain durian shell fiber- Fe_3O_4 (DF).

3.2.3. Preparation of Durian Shell Fiber- Fe_3O_4 MOF (DFM)

The preparation of durian shell fiber- Fe_3O_4 MOF composite material was carried out by the self-assembly method. Firstly, 0.05g of the prepared DF was dispersed ultrasonically and added to 4 mL $\text{FeCl}_3 \cdot 6\text{H}_2\text{O}$ ethanol solution (10 mmol/L) for 15 min, then dispersed in 4 mL of H_3BTC ethanol solution (10 mmol/L), and heated at 70°C for 30 min. Each step was separated with a strong permanent magnet and washed with ethanol. After a certain number of $\text{FeCl}_3 \cdot 6\text{H}_2\text{O}/\text{H}_3\text{BTC}$ cycles, the sample was recovered with a permanent magnet and washed with ethanol/water, and then vacuum dried at 60°C for 12 h to obtain DFM. The synthetic process of DFM preparation can be seen in Scheme 1. The obtained samples at different cycles (0, 10, 20, and 40) were named DF, DFM-10, DFM-20, and DFM-40, respectively.



Scheme 1. The synthetic process of DFM preparation.

3.3. Adsorption Properties

In the adsorption experiment, the MB stock solution had a concentration of 100 mg/L. It was stored in a dark place and diluted to 2.5–20 mg/L when used. The MB adsorption experiment was carried out in a constant-temperature shaker. The specific experiment was as follows: The adsorbent (5 mg) was mixed with 15 mL MB solutions of different initial concentrations and placed in constant-temperature oscillator at 25 °C. After a reaction time of 3 h, the adsorbent material was collected with a magnet. MB concentration in the supernatants was measured at 664 nm by using a UV-Vis spectrophotometer. The quantity of adsorption (Q_e (mg/g)) and rate of removing MB (R (%)) were calculated based on the following equations:

$$Q_e = \frac{(C_0 - C_e) \times V}{m} \quad (12)$$

$$R = \frac{C_0 - C_e}{C_0} \times 100\% \quad (13)$$

where C_0 (mg/L) is the initial concentrations of MB and C_e (mg/L) is the equilibrium concentrations of MB; m is determined to the weight of adsorbent (g), and V is defined as the volume of the liquid solution (mL) [58,59].

3.4. Characterization

FTIR spectra of the sample was performed with an FTIR spectrometer (AVATAR 360, Nicole company, MA, USA). A minimum of 32 scans was signal-averaged with a resolution of 2 cm^{-1} in the $4000\text{--}400 \text{ cm}^{-1}$ ranges. X-ray diffraction (XRD) analysis of the material was conducted on X-ray powder diffraction (XRD-6100, Shimadzu company, Kyoto, Japan) with a scanning rate of $5^\circ/\text{min}$. The morphology of the as-prepared adsorbent was characterized by scanning electron microscope (SEM, S-4800, Hitachi company, Kyoto, Japan). Transmission electron microscopy (TEM) analysis was undertaken on a JEM-1400 UV-Vis spectrophotometer (UV-2450, Shimadzu Company, Kyoto, Japan). The zeta potential of material was tested by using a Zeta potential analyzer (Zetasizer Nano ZS90, Malvern Instruments Ltd., Malvern, UK). Total organic carbon (TOC) was obtained by total organic carbon analyzer (Shimadzu, Kyoto, Japan).

4. Conclusions

In this work, durian shell biomass carbon fiber and Fe_3O_4 functionalized metalorganic framework composite material (DFM) was prepared and the structure was characterized. Compared with conventional adsorbents, it can effectively remove MB from wastewater. Then, comparing the adsorption capacity with different adsorbents to MB, it can be seen that DFM-10 had the best effect and the maximum adsorption capacity for MB was 53.31 mg/g. Adsorption isotherms studies showed that DFM-10 is more in line with the Langmuir isotherm model, adsorption kinetics studies showed that DFM-10 is more in line with the pseudo-second-order kinetic model, and thermodynamic analysis showed that DFM-10 adsorbs MB in an aqueous spontaneous endothermic physical adsorption process. This study proposes an effective method to prepare DFM composite material, which has high adsorption efficiency and can be recycled, and is expected to be widely used to removing MB in wastewater.

Supplementary Materials: The following supporting information can be downloaded at <https://www.mdpi.com/article/10.3390/ijms23115900/s1>. References [52–57] are cited in supplementary materials.

Author Contributions: Conceptualization, methodology, and formal analysis were done by Z.C., Q.L. and H.L.; material characterization were done by J.W., G.T. and F.W.; writing—original draft preparation, resources, supervision, and funding acquisition were done by J.H., Y.Z. and G.W. All authors have read and agreed to the published version of the manuscript.

Funding: This work was financially supported by The Natural Science Foundation of the Jiangsu Higher Education Institutions of China (21KJB530010), Jiangsu Planned Projects for Postdoctoral Research Funds (2020Z098), Opening Project of Guangxi Key Laboratory of Petrochemical Resource Processing and Process Intensification Technology (2021K006), Jiangsu Key Laboratory of Advanced Catalytic Materials and Technology (JLCT202107), and Start-up Fund from Nanjing Forestry University and the Analysis and Test Center of Nanjing Forestry University.

Institutional Review Board Statement: Not applicable.

Informed Consent Statement: Not applicable.

Data Availability Statement: The data presented in this study are available on request from the corresponding author.

Acknowledgments: We thank “National Positioning Observation Station of Hung-tse Lake Wetland Ecosystem in Jiangsu Province, Hongze 223100, China” for their generous assistance with the support of the experiment.

Conflicts of Interest: The authors declare that they have no known competing financial interests or personal relationships that could have appeared to influence the work reported in this paper.

Sample Availability: Samples of the compounds are not available from the authors.

References

1. Qiu, J.; Feng, Y.; Zhang, X.; Jia, M.; Yao, J. Acid-promoted synthesis of UiO-66 for highly selective adsorption of anionic dyes: Adsorption performance and mechanisms. *J. Colloid Interface Sci.* **2017**, *499*, 151–158. [[CrossRef](#)] [[PubMed](#)]
2. Reynel, H.E.; Mendoza, D.I.; Bonilla, A. Relevance of anionic dye properties on water decolorization performance using bone char: Adsorption kinetics, isotherms and breakthrough curves. *J. Mol. Liq.* **2016**, *219*, 425–434. [[CrossRef](#)]
3. Atrous, M.; Sellaoui, L.; Bouzid, M.; Lima, E.C.; Thue, P.S.; Bonilla-Petriciolet, A.; Ben Lamine, A. Adsorption of dyes acid red 1 and acid green 25 on grafted clay: Modeling and statistical physics interpretation. *J. Mol. Liq.* **2019**, *294*, 111610. [[CrossRef](#)]
4. Rashid, J.; Tehreem, F.; Rehman, A.; Kumar, R. Synthesis using natural functionalization of activated carbon from pumpkin peels for decolorization of aqueous methylene blue. *Sci. Total Environ.* **2019**, *671*, 369–376. [[CrossRef](#)]
5. Wu, G.; Xing, W. Fabrication of ternary visible-light-driven semiconductor photocatalyst and its effective photocatalytic performance. *Mater. Technol.* **2018**, *34*, 292–300. [[CrossRef](#)]
6. Hassan, M.M.; Carr, C.M. A critical review on recent advancements of the removal of reactive dyes from dyehouse effluent by ion-exchange adsorbents. *Chemosphere* **2018**, *209*, 201–219. [[CrossRef](#)]
7. Wu, G.; Liu, Q.; Wang, J.; Cai, Z.; Li, H.; Zhang, T.; Lu, R.; Li, P.; Han, J.; Xing, W. Synthesis of silver-based composite photocatalysis material and its visible-light-driven photocatalytic degradation of dye pollutants. *Fresenius Environ. Bull.* **2021**, *30*, 9696–9706.
8. Huang, X.; Wei, D.; Zhang, X.; Fan, D.; Sun, X.; Du, B.; Wei, Q. Synthesis of amino-functionalized magnetic aerobic granular sludge-biochar for Pb(II) removal: Adsorption performance and mechanism studies. *Sci. Total Environ.* **2019**, *685*, 681–689. [[CrossRef](#)]
9. Wu, G.; Ma, F.; Xiong, R.; Xu, Z.; Li, P.; Han, J.; Xing, W. Fabrication of semiconductor photocatalyst and its high photo-catalytic performance under visible light irradiation. *Fresenius Env. Bull.* **2021**, *30*, 10482–10491.
10. AliYounis, S.; Maitlo, H.A.; Lee, J.; Kim, K.-H. Nanotechnology-based sorption and membrane technologies for the treatment of petroleum-based pollutants in natural ecosystems and wastewater streams. *Adv. Colloid Interface Sci.* **2019**, *275*, 102071. [[CrossRef](#)]
11. Wu, G.; Liu, Q.; Wang, J.; Zhang, Y.; Yu, C.; Bian, H.; Hegazy, M.; Han, J.; Xing, W. Facile fabrication of Bi₂WO₆/biochar composites with enhanced charge carrier separation for photodecomposition of dyes. *Colloids Surf. A Physicochem. Eng. Asp.* **2021**, *634*, 127945. [[CrossRef](#)]
12. Wu, G.; Xing, W.; Han, J.; Li, P. Fabrication of silver-based visible-light-driven photocatalyst and degradation of organic pollutions in wastewater. *Fresenius Env. Bull.* **2020**, *29*, 445–453.
13. Filote, C.; Volf, I.; Santos, S.C.R.; Botelho, C.M.S. Bioadsorptive removal of Pb(II) from aqueous solution by the biore-finery waste of *Fucus spiralis*. *Sci. Total Environ.* **2019**, *648*, 1201–1209. [[CrossRef](#)]
14. Xing, W.; Zhang, Y.; Cheng, K.; Zou, J.; Wu, G. Fabrication of novel carbon species into porous g-C₃N₄ nanosheet frameworks with enhanced photocatalytic performance. *New J. Chem.* **2021**, *45*, 10589–10593. [[CrossRef](#)]
15. Jawad, A.H.; Mubarak, N.S.A.; Abdulhameed, A.S. Hybrid Crosslinked Chitosan-Epichlorohydrin/TiO₂ Nanocomposite for Reactive Red 120 Dye Adsorption: Kinetic, Isotherm, Thermodynamic, and Mechanism Study. *J. Polym. Environ.* **2020**, *28*, 624–637. [[CrossRef](#)]
16. Tran, T.H.; Le, A.H.; Pham, T.H.; Nguyen, D.T.; Chang, S.W.; Chung, W.J. Adsorption isotherms and kinetic modeling of methylene blue dye onto a carbonaceous hydrochar adsorbent derived from coffee husk waste. *Sci. Total Environ.* **2020**, *725*, 138325. [[CrossRef](#)]

17. Maksoud, M.I.A.A.; Elgarahy, A.M.; Farrell, C.; Al-Muhtaseb, A.H.; Rooney, D.W.; Osman, A.I. Insight on water remediation application using magnetic nanomaterials and biosorbents. *Coord. Chem. Rev.* **2020**, *403*, 213096. [[CrossRef](#)]
18. Hasanzadehab, M.; Simchi, A.; Far, H.S. Nanoporous composites of activated carbon-metal organic frameworks for organic dye adsorption: Synthesis, adsorption mechanism and kinetics studies. *J. Ind. Eng. Chem.* **2019**, *81*, 405–414. [[CrossRef](#)]
19. Thines, K.; Abdullah, E.C.; Mubarak, N.; Ruthiraan, M. Synthesis of magnetic biochar from agricultural waste biomass to enhancing route for waste water and polymer application: A review. *Renew. Sustain. Energy Rev.* **2017**, *67*, 257–276. [[CrossRef](#)]
20. Lai, F.; Miao, Y.-E.; Zuo, L.; Lu, H.; Huang, Y.; Liu, T. Biomass-Derived Nitrogen-Doped Carbon Nanofiber Network: A Facile Template for Decoration of Ultrathin Nickel-Cobalt Layered Double Hydroxide Nanosheets as High-Performance Asymmetric Supercapacitor Electrode. *Small* **2016**, *12*, 3235–3244. [[CrossRef](#)]
21. Xing, W.; Liu, Q.; Wang, J.; Xia, S.; Ma, L.; Lu, R.; Zhang, Y.; Huang, Y.; Wu, G. High Selectivity and Reusability of Bi-omass-Based Adsorbent for Chloramphenicol Removal. *Nanomaterials* **2021**, *11*, 2950. [[CrossRef](#)] [[PubMed](#)]
22. Zhang, C.; Zeng, G.; Huang, D.; Lai, C.; Chen, M.; Cheng, M.; Tang, W.; Tang, L.; Dong, H.; Huang, B.; et al. Biochar for environmental management: Mitigating greenhouse gas emissions, contaminant treatment, and potential negative impacts. *Chem. Eng. J.* **2019**, *373*, 902–922. [[CrossRef](#)]
23. Son, E.-B.; Poo, K.-M.; Chang, J.-S.; Chae, K.-J. Heavy metal removal from aqueous solutions using engineered magnetic biochars derived from waste marine macro-algal biomass. *Sci. Total Environ.* **2018**, *615*, 161–168. [[CrossRef](#)]
24. Luo, M.-T.; Zhao, C.; Huang, C.; Chen, X.-F.; Huang, Q.-L.; Qi, G.-X.; Tian, L.-L.; Xiong, L.; Li, H.-L.; Chen, X.-D. Efficient Using Durian Shell Hydrolysate as Low-Cost Substrate for Bacterial Cellulose Production by *Gluconacetobacter xylinus*. *Indian J. Microbiol.* **2017**, *57*, 393–399. [[CrossRef](#)]
25. Yazidi, A.; Atrous, M.; Soetaredjo, F.E.; Sellaoui, L.; Ismajji, S.; Erto, A.; Bonilla-Petriciolet, A.; Dotto, G.L.; Ben Lamine, A. Adsorption of amoxicillin and tetracycline on activated carbon prepared from durian shell in single and binary systems: Experimental study and modeling analysis. *Chem. Eng. J.* **2019**, *379*, 122320. [[CrossRef](#)]
26. Laysandra, L.; Santosa, F.H.; Austen, V.; Soetaredjo, F.E.; Foe, K.; Putro, J.N.; Ju, Y.H.; Ismajji, S. Rarasapo-nin-bentonite-activated biochar from durian shells composite for removal of crystal violet and Cr(VI) from aqueous solution. *Environ. Sci. Pollut. Res.* **2018**, *25*, 30680–30695. [[CrossRef](#)]
27. Kurniawan, A.; Sisnandy, V.O.A.; Trilestari, K.; Sunarso, J.; Indraswati, N.; Ismajji, S. Performance of durian shell waste as high capacity biosorbent for Cr(VI) removal from synthetic wastewater. *Ecol. Eng.* **2011**, *37*, 940–947. [[CrossRef](#)]
28. Yang, Q.; Zhao, Q.; Ren, S.; Lu, Q.; Guo, X.; Chen, Z. Fabrication of core-shell Fe₃O₄@MIL-100(Fe) magnetic microspheres for the removal of Cr(VI) in aqueous solution. *J. Solid State Chem.* **2016**, *244*, 25–30. [[CrossRef](#)]
29. Zheng, X.; Wang, J.; Xue, X.; Liu, W.; Kong, Y.; Cheng, R.; Yuan, D. Facile synthesis of Fe₃O₄@MOF-100(Fe) magnetic microspheres for the adsorption of diclofenac sodium in aqueous solution. *Environ. Sci. Pollut. Res.* **2018**, *25*, 31705–31717. [[CrossRef](#)]
30. Luu, Q.S.; Do, U.T.; Kim, D.; Kim, J.; Jo, D.; Nguyen, Q.T.; Lee, Y. Enhancing adsorption efficiencies of organic molecules through covalently bonded structures of magnetic carbon nanoparticles. *J. Ind. Eng. Chem.* **2021**, *105*, 74–82. [[CrossRef](#)]
31. Wu, G.; Liu, Q.; Wang, J.; Xia, S.; Wu, H.; Zong, J.; Han, J.; Xing, W. Facile fabrication of rape straw biomass fi-ber/ β -CD/Fe₃O₄ as adsorbent for effective removal of ibuprofen. *Ind. Crops. Prod.* **2021**, *173*, 114150. [[CrossRef](#)]
32. Sun, Y.; Ni, P.Y.; Zhu, M.Y.; Yao, Y.L.; Fu, S.W. Preparation of Fe₃O₄@C submicron rods for adsorption of methylene blue and fast separation from water. *Micro. Nano Lett.* **2019**, *14*, 962–966. [[CrossRef](#)]
33. Rajput, S.; Pittman, C.U., Jr.; Mohan, D. Magnetic magnetite (Fe₃O₄) nanoparticle synthesis and applications for lead (Pb²⁺) and chromium (Cr⁶⁺) removal from water. *J. Colloid Interface Sci.* **2016**, *468*, 334–346. [[CrossRef](#)]
34. Wang, J.; Zhao, G.; Yu, F. Facile preparation of Fe₃O₄@MOF core-shell microspheres for lipase immobilization. *J. Taiwan Inst. Chem. Eng.* **2016**, *69*, 139–145. [[CrossRef](#)]
35. Su, M.; Fang, Y.; Li, B.; Yin, W.; Gu, J.; Liang, H.; Li, P.; Wu, J. Enhanced hexavalent chromium removal by activated carbon modified with micro-sized goethite using a facile impregnation method. *Sci. Total Environ.* **2018**, *647*, 47–56. [[CrossRef](#)]
36. Sun, X.; Gao, G.; Yan, D.; Feng, C. Synthesis and electrochemical properties of Fe₃O₄@MOF core-shell microspheres as an anode for lithium ion battery application. *Appl. Surf. Sci.* **2017**, *405*, 52–59. [[CrossRef](#)]
37. Abdi, J.; Vossoughi, M.; Mahmoodi, N.M.; Alemzadeh, I. Synthesis of metal-organic framework hybrid nanocomposites based on GO and CNT with high adsorption capacity for dye removal. *Chem. Eng. J.* **2017**, *326*, 1145–1158. [[CrossRef](#)]
38. Lin, K.Y.A.; Liu, Y.T.; Chen, S.Y. Adsorption of fluoride to UiO-66-NH₂ in water: Stability, kinetic, isotherm and thermodynamic studies. *J. Colloid Interf. Sci.* **2016**, *461*, 79–87. [[CrossRef](#)]
39. Efome, J.E.; Rana, D.; Matsuura, T.; Lan, C.Q. Insight Studies on Metal-Organic Framework Nanofibrous Membrane Adsorption and Activation for Heavy Metal Ions Removal from Aqueous Solution. *ACS Appl. Mater. Interfaces* **2018**, *10*, 18619–18629. [[CrossRef](#)]
40. Xia, L.J.; Zhou, S.J.; Zhang, C.H.; Fu, Z.A.; Wang, A.M.; Zhang, Q.; Wang, Y.L.; Liu, X.; Wang, X.G.; Xu, W.L. En-vironment-friendly *Juncus effusus*-based adsorbent with a three-dimensional network structure for highly efficient removal of dyes from wastewater. *J. Clean Prod.* **2020**, *259*, 120812. [[CrossRef](#)]
41. Liang, S.; Shi, S.; Zhang, H.; Qiu, J.; Yu, W.; Li, M.; Gan, Q.; Yu, W.; Xiao, K.; Liu, B.; et al. One-pot solvothermal synthesis of magnetic biochar from waste biomass: Formation mechanism and efficient adsorption of Cr(VI) in an aqueous solution. *Sci. Total Environ.* **2019**, *695*, 133886. [[CrossRef](#)]

42. Zhou, Y.; Liu, X.; Xiang, Y.; Wang, P.; Zhang, J.; Zhang, F.; Wei, J.; Luo, L.; Lei, M.; Tang, L. Modification of biochar derived from sawdust and its application in removal of tetracycline and copper from aqueous solution: Adsorption mechanism and modelling. *Bioresour. Technol.* **2017**, *245*, 266–273. [[CrossRef](#)]
43. Dong, H.; Deng, J.; Xie, Y.; Zhang, C.; Jiang, Z.; Cheng, Y.; Hou, K.; Zeng, G. Stabilization of nanoscale zero-valent iron (nZVI) with modified biochar for Cr(VI) removal from aqueous solution. *J. Hazard. Mater.* **2017**, *332*, 79–86. [[CrossRef](#)]
44. Han, Y.; Cao, X.; Ouyang, X.; Sohi, S.; Chen, J. Adsorption kinetics of magnetic biochar derived from peanut hull on removal of Cr(VI) from aqueous solution: Effects of production conditions and particle size. *Chemosphere* **2016**, *145*, 336–341. [[CrossRef](#)]
45. Fan, S.; Wang, Y.; Wang, Z.; Tang, J.; Tang, J.; Li, X. Removal of methylene blue from aqueous solution by sewage sludge-derived biochar: Adsorption kinetics, equilibrium, thermodynamics and mechanism. *J. Environ. Chem. Eng.* **2017**, *5*, 601–611. [[CrossRef](#)]
46. Ahmed, M.B.; Zhou, J.L.; Ngo, H.H.; Guo, W.; Johir, M.A.H.; Sornalingam, K. Single and competitive sorption properties and mechanism of functionalized biochar for removing sulfonamide antibiotics from water. *Chem. Eng. J.* **2017**, *311*, 348–358. [[CrossRef](#)]
47. Yap, M.W.; Mubarak, N.M.; Sahu, J.N.; Abdullah, E.C. Microwave induced synthesis of magnetic biochar from agri-cultural biomass for removal of lead and cadmium from wastewater. *J. Ind. Eng. Chem.* **2017**, *45*, 287–295. [[CrossRef](#)]
48. Yuan, J.; Zhu, Y.; Wang, J.; Gan, L.; He, M.; Zhang, T.; Li, P.; Qiu, F. Preparation and application of Mg–Al composite oxide/coconut shell carbon fiber for effective removal of phosphorus from domestic sewage. *Food Bioprod. Process.* **2021**, *126*, 293–304. [[CrossRef](#)]
49. Sewu, D.D.; Boakye, P.; Woo, S.H. Highly efficient adsorption of cationic dye by biochar produced with Korean cabbage waste. *Bioresour. Technol.* **2017**, *224*, 206–213. [[CrossRef](#)]
50. Eren, E.; Cubuk, O.; Ciftci, H.; Eren, B.; Caglar, B. Adsorption of basic dye from aqueous solutions by modified sepiolite: Equilibrium, kinetics and thermodynamics study. *Desalination* **2010**, *252*, 88–96. [[CrossRef](#)]
51. Xu, Y.; Jin, J.; Li, X.; Song, C.; Meng, H.; Zhang, X. Adsorption behavior of methylene blue on Fe₃O₄-embedded hybrid magnetic metal–organic framework. *Desalination Water Treat.* **2016**, *57*, 25216–25225. [[CrossRef](#)]
52. Cai, X.; Li, J.; Liu, Y.; Hu, X.; Tan, X.; Liu, S.; Wang, H.; Gu, Y.; Luo, L. Design and Preparation of Chitosan-Crosslinked Bismuth Ferrite/Biochar Coupled Magnetic Material for Methylene Blue Removal. *Int. J. Environ. Res. Public Health.* **2020**, *17*, 6. [[CrossRef](#)]
53. Li, Y.; Zhang, Y.; Zhang, Y.; Wang, G.; Li, S.; Han, R.; Wei, W. Reed biochar supported hydroxyapatite nanocomposite: Characterization and reactivity for methylene blue removal from aqueous media. *J. Mol. Liq.* **2018**, *263*, 53–63. [[CrossRef](#)]
54. Aslam Malana, M.; Parveen, S.; Beenish Qureshi, R. Adsorptive removal of organic dyes from aqueous solutions using acrylic acid-acrylonitrile-N-isopropylacrylamide polymeric gels as adsorbents: Linear and non linear isotherms. *Desalination Water Treat.* **2016**, *57*, 22543–22550. [[CrossRef](#)]
55. Hoslett, J.; Ghazal, H.; Mohamad, N.; Jouhara, H. Removal of methylene blue from aqueous solutions by biochar prepared from the pyrolysis of mixed municipal discarded material. *Sci. Total Environ.* **2020**, *714*, 136832. [[CrossRef](#)]
56. Gao, Y.; Sun, D.; Han, C.; Huang, J. Comprehensive Utilization of Phosphogypsum: Adsorption of Methylene Blue and its Application in Bricks. *Surf. Rev. Lett.* **2021**, *28*, 2150075. [[CrossRef](#)]
57. Wanyonyi, W.C.; Onyari, J.M.; Shiundu, P.M. Adsorption of methylene blue dye from aqueous solutions using eichhornia crassipes. *Bull. Environ. Contam. Toxicol.* **2013**, *91*, 362–366. [[CrossRef](#)]
58. Liu, Z.; Yang, W.; Xu, W.; Liu, Y. Removal of elemental mercury by bio-chars derived from seaweed impregnated with potassium iodine. *Chem. Eng. J.* **2018**, *339*, 468–478. [[CrossRef](#)]
59. Selvaraju, G.; Abu Bakar, N.K. Production of a new industrially viable green-activated carbon from Artocarpus integer fruit processing waste and evaluation of its chemical, morphological and adsorption properties. *J. Clean. Prod.* **2016**, *141*, 989–999. [[CrossRef](#)]